Peer-reviewed version available at *Fluids* **2020**, *5*, 72; doi:10.3390/fluids5020072

Article

Jet Oscillation Frequency Characterization of a Sweeping Jet Actuator

Furkan Oz [1] and Kursat Kara [1,*]

[1] School of Mechanical and Aerospace Engineering, Oklahoma State University, Stillwater, OK 74078, USA
* Correspondence: kursat.kara@okstate.edu ; Tel.: +1-405-744-6579; Fax: +1-405-744-7873

Abstract: The time-resolved flowfield of a spatially oscillating jet emitted by a Sweeping Jet (SWJ) actuator is investigated numerically using three-dimensional Reynolds-averaged Navier-Stokes (3D-URANS) equations. Numerical simulations are performed for a practical range of mass flow rates providing flow conditions ranging from incompressible to subsonic compressible flows. A linear relationship between the mass flow rate and the jet oscillation frequency is found ($f = 40.5\dot{m} + 39.9$, $R^2 = 0.983$). The results of the numerical model are compared with the experimental data in the literature, and good agreement is found. Additionally, it is observed that the SWJ actuator frequency response switches from one linear mode to another linear mode when the compressibility effects become important.

Keywords: Sweeping jet actuator; Jet oscillation frequency; Compressibility effect; Unsteady Reynolds–Averaged Navier–Stokes; Mass flow rate

1. Introduction

Active flow control (AFC) has been a popular research topic since its discovery in the 1950s. In earlier applications, researches are mainly focused on to reduce the takeoff and landing speed of military aircraft. The development and application of the AFC technologies for commercial platforms accelerated in the 2000s, and several programs are initiated. As an example, the NASA Environmentally Responsible Aviation (ERA) project is focused on developing technologies to reduce noise level and fuel consumption of future aircraft by employing AFC technology [1]. Boeing's ecoDemonstrator 757 [2] is another example of the utilization of AFC and sweeping jet (SWJ) actuator in commercial platforms to enhance the aerodynamic efficiency of a vertical tail [3].

Fluidic actuators employed in AFC increase the momentum of the local flow field by fluid injection or suction. The SWJ actuator is a fluidic actuator. It generates a self-induced self-sustaining oscillating jet flow field due to its interior geometric design. Figure 1 shows the schematics of the SWJ actuator used in the present study. Historically, SWJ actuators are employed in many applications such as windshield-washer fluid nozzle [4] and flow-metering devices [5,6]. Recently, SWJ actuators have been explored in several numerical and experimental studies [7–35]. Aerodynamic performance improvements up to 60% were reported in active flow control studies, namely, a single-element high-lift airfoil [36], a V-22 wing-nacelle combination [37], and wind turbine blades [38]. The SWJ actuators successfully reduced the drag force on trucks [39] and bluff bodies [40] and suppressed the flow separation bubble [41]. Moreover, the side force was increased by 50-70% on a typical twin-engine aircraft whose vertical tail has multiple SWJ actuators operating at Reynolds numbers up to 1.5 million [42].

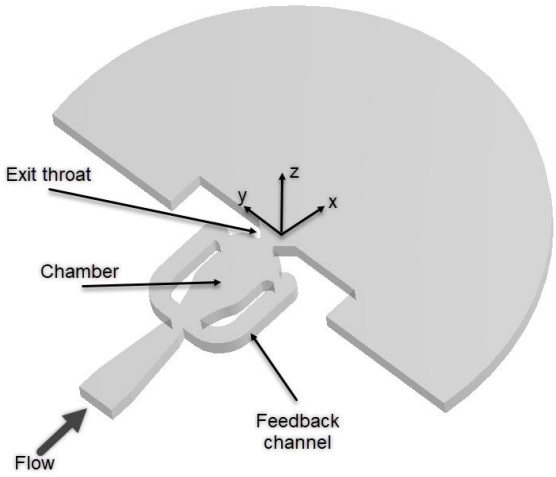

Figure 1. A schematic of the sweeping jet actuator and computational domain.

Although there is an increasing interest in using SWJ actuators as AFC devices in various engineering applications, the fundamental flow physics and working principles of the SWJ actuator and design parameters are still investigated numerically and experimentally. In a recent experimental study conducted at the NASA Langley 15-Inch Low-Speed tunnel, several actuator parameters were investigated, including blowing coefficients, operation mode, pitch and spreading angles, and actuator size [43]. The results indicate that the SWJ actuators are more effective than other well-known flow control techniques such as steady blowing and steady vortex-generating jets. Internal dynamics of SWJ actuators were investigated using a high-speed camera, and two different SWJ actuators were characterized based on their jet oscillation frequency and mass flow rate [44]. The jet oscillation process was shown in detail at 650 Hz and 1250 Hz. The results showed the effect of compressibility on the oscillation frequency and deviation from the linear trend line. In another study, the high-frequency characterization of an SWJ actuator was performed experimentally above 500 Hz [45]. The acoustic field of SWJ actuators also measured at full- and half-scale [46]. The findings suggested that rougher internal surfaces with 3D printed actuators resulted in higher sweep frequency. The effects of SWJ actuator geometry on the jet oscillation frequency was studied numerically for incompressible flows [47]. The authors confirmed that the effect of feedback channel length on the oscillation frequency is negligible. However, the results showed that a longer chamber length results in a lower frequency.

Although some studies examined the effect of mass flow rate on the SWJ actuator oscillation frequency, an analysis considering full subsonic regime, including incompressible and compressible flows, was not found in the literature. In the present study, we use a three-dimensional unsteady Reynolds-Averaged Navier-Stokes analysis to investigate the jet oscillation frequency of the SWJ actuator for mass flow rate and total-to-static pressure ratio. Based on the analysis results, we recommend functions to predict jet oscillation frequency. It is expected that the model developed here could help with the design of the SWJ actuator for flow control applications.

2. Numerical Methodology and Problem Setup

For the current numerical modeling, the geometry of the SWJ actuator considered in the previous computational and experimental studies [9,17,41,48] is adopted. The schematic of the SWJ actuator employed and the three-dimensional (3D) computational domain is presented in Fig. 1. The x-axis corresponds to the streamwise direction, the y-axis corresponds to the spanwise direction, and z-axis corresponds to the vertical direction. The computational domain is symmetric about the x-axis. The SWJ actuator has a chamber, an exit nozzle, and two feedback channels. The exit nozzle size, h, is chosen as a length scale. In the present study, the exit nozzle throat aspect ratio (h/d) is 1 and the exit throat height is h=6.35 mm. The flow inlet to the exit nozzle throat area ratio is 2.5531.

The fluid flow through a 3D SWJ actuator is numerically modeled by using a commercial computational fluid dynamics (CFD) code, Ansys Fluent v17, which employs a control volume method to discretize the Reynolds-Averaged Navier-Stokes (RANS) equations with second-order accuracy. The PISO algorithm is used for unsteady calculations with a second-order fully implicit scheme for time integration. The working fluid is air. The density is calculated from the ideal gas law. The viscosity is evaluated using Sutherland's law using the reference viscosity $\mu_0 = 1.716\times10^{-5}$ kg/(m-s), reference temperature T_0 = 273.16 K, and effective temperature S = 110.56 K. The ambient static pressure is assumed as the reference pressure and set to 101,325 Pa. The ambient static temperature is 288.16 K. The flow parameters at the SWJ actuator inlet boundary with varying mass-flow rates and total to static pressure ratios are given in Table 1. A fully turbulent flow is assumed at the inlet. The turbulence intensity at the inlet is 5%, and the turbulent length scale is 1 mm. Similar to earlier studies [41,49], shear-stress transport SST k-ω turbulence model is employed.

For unsteady analyses, a constant time step size is set to $\Delta t=1\times10^{-5}$ s (210 time-steps per jet oscillation cycle for $\dot{m}$ = 11.3398 kg/s) to capture the jet oscillations from the SWJ actuator. The solution does not change with a further reduction of the time step. Previous studies documented that increasing the mass flow rate increases the jet oscillation frequency [9,48], and therefore, the same time-step size is used in all simulations. To obtain a fully developed oscillatory flow, each computation is at first initialized with a constant mass flow rate at the inlet boundary, and an unsteady simulation is run for 10,000 time-steps (0.1 s, or approximately 50 periods for $\dot{m}$ = 11.3398 kg/s). Then, the unsteady simulation is run for another 10,000 time-steps to record time statistics, resulting in a 20,000 time-steps for each simulation. The maximum number of sub-iterations per time-step is set to 20.

Table 1. Inflow boundary conditions.

$\dot{m}$ (g/s)	0.4536	1.1340	2.2680	4.5359	6.8039	9.0718	11.3398
p_0/p_∞	1.002	1.009	1.034	1.121	1.251	1.471	1.728

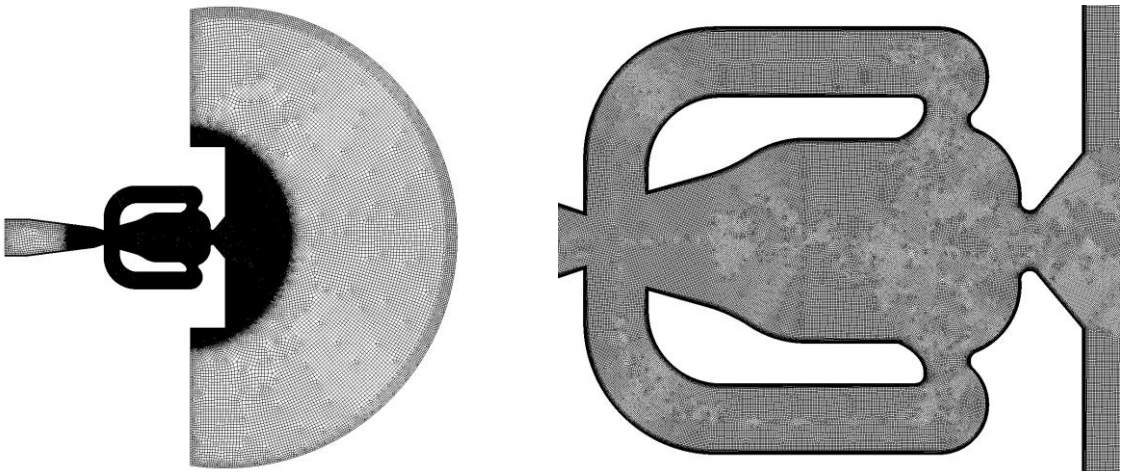

(a) (b)

Figure 2. Computational mesh (N40). a) computational domain and b) the sweeping jet actuator.

The computational mesh is created using the Ansys Meshing software by employing hexagonal mesh elements. Figure 2 shows the computational mesh. The element size is determined based on the characteristic length, h. The boundary layer is resolved using 25 layers in the wall-normal direction with a growth rate of 1.1, as presented in the reference [41]. The first point of the wall is placed at 0.0127 mm (h/500) in the wall-normal direction. The y^+ values of the resulting mesh are less than one. To generate the coarse mesh, the element size is assumed to be h/10, and the resulting mesh has 60 elements across the exit throat nozzle, including 25 elements for each wall and ten elements to fill the space between the boundary layer meshes. This mesh is named N10, referring to

the number of elements (N=10) to fill the space between the boundary layer meshes. The element size in the z-direction is assumed to be h/10.

To control the element size, two levels of refinement are applied using the sphere of influence method with sphere radii of 8h and 20h. The maximum element size for the outer sphere is set to N5. For the inner sphere, the element size can be changed from N10 to N80. To perform mesh sensitivity analysis, the number of elements is successively increased, and four different meshes are created resulting in coarse, normal, fine, and finest meshes. The mesh parameters are given in Table 2. The finest mesh (N80) has 130 elements across the exit nozzle throat, and the resulting mesh has 6.7 million elements. We evaluated the sensitivity of numerical calculations to the mesh size given in Table 2 by employing the numerical model described above to determine adequate mesh resolution. The results of the mesh sensitivity analysis are presented in the next section.

Table 2. Computational mesh parameters

Mesh Name	Element Size (mm)	Number of Elements	Mesh Resolution
N10	6.3500E-01	397,670	Coarse
N20	3.1750E-01	749,280	Normal
N40	1.5875E-01	2,023,860	Fine
N80	7.9375E-02	6,672,820	Finest

3. Results

3.1. Mesh Sensitivity Analysis

Performing a mesh sensitivity analysis is critically important to minimize spatial discretization errors and computational cost. In this study, four different meshes are employed, and their parameters are presented in Table 2. The coarse mesh (N10) has approximately 0.4 million elements, and the finest mesh (N80) has approximately 6.7 million elements. Using the numerical model described in the previous section, a set of time-accurate simulations are performed using a mass flow rate of 6.8039 g/s for all the meshes listed in Table 2. The time-averaged velocity profile along the SWJ actuator symmetry line (x-axis) is presented in Figure 3. In the figure, the velocity is non-dimensionalized by the maximum velocity at the SWJ actuator exit nozzle throat. The peak velocity of the finest mesh (N80) is 172.7 m/s. The coarse mesh (N10) result at the same location has a 1.9% deviation (3.3 m/s), as shown in Figure 3-b. There is no discernible difference between the results of N40 and N80, indicating that the independent mesh results are obtained for the mesh N40. Besides, time-averaged static pressure and temperature profiles along the symmetry line are presented in Figure 4. The results are non-dimensionalized with free stream values, e.g., P_∞ = 101,325 Pa and T_∞ = 288.16 K. The pressure and temperature profiles converge to N80 results with increased mesh resolution. There is no visible difference in the results between N40 and N80 meshes. Time-averaged velocity contours are compared for the coarse and the finest meshes in Figure 5. For an easy comparison, the same contour levels are used in the figures. Figure 5 (a) shows that the flow velocity in the feedback channel and actuator inlet are overpredicted, but at the exit nozzle, it was underpredicted in the coarse mesh simulation. To perform a detailed comparison, velocity profiles are plotted at various downstream locations in Figure 6. At the SWJ exit nozzle throat, all the results follow the same trend. However, the coarse and normal mesh profiles deviate from the fine mesh results. The coarse mesh simulation underestimates velocity at y/h=±0.35 locations. The simulation using the normal mesh underestimates the velocity at y/h=0.35 but slightly overestimates elsewhere. The differences among the velocity profiles become clearer at further downstream locations, as shown in Figure 6 (b-d). The double velocity peak is only visible in the fine and very fine meshes. The velocity profile of normal mesh (N20) shifted for all locations. The coarse mesh (N10) and normal mesh (N20) fail to capture the peak velocity, jet width, and direction. Up to this point, we compared the time-averaged results for various mesh resolutions and found that the fine mesh (N40)

Preprints (www.preprints.org) | NOT PEER-REVIEWED | Posted: 26 February 2020 doi:10.20944/preprints202002.0384.v1

Peer-reviewed version available at Fluids 2020, 5, 72; doi:10.3390/fluids5020072

can capture the time-averaged flow quantities. In the next paragraph, comparisons for time-accurate simulations will be presented.

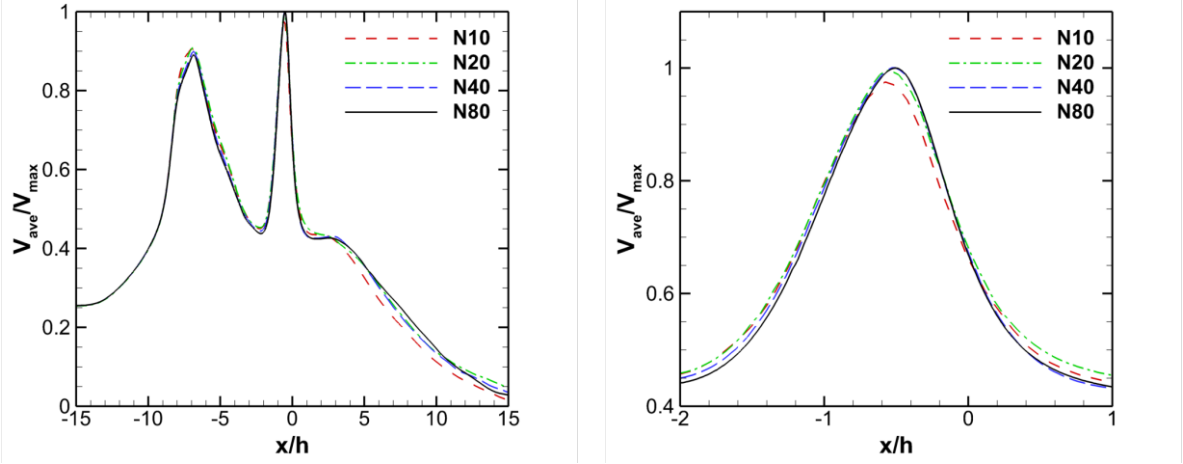

Figure 3. Time-averaged velocity magnitude along the SWJ actuator centerline.

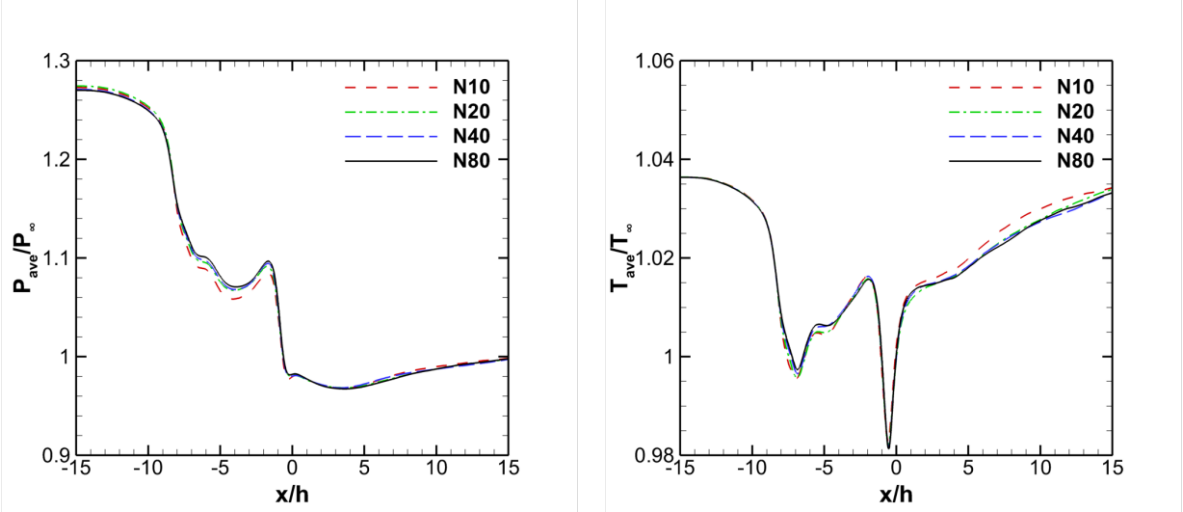

Figure 4. Time-averaged static-to-reference pressure and temperature ratio along the centerline.

Peer-reviewed version available at Fluids 2020, 5, 72; doi:10.3390/fluids5020072

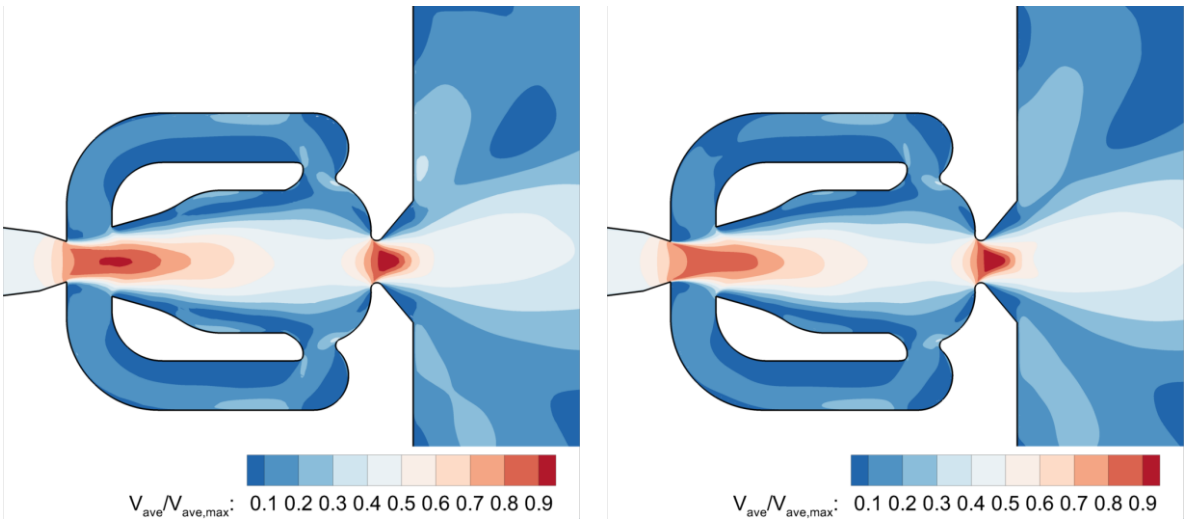

(a) (b)

Figure 5. Time averaged velocity magnitude contour on z=0 plane for (a) N10 $V_{ave,max}$ = 169.4 and (b) N80 $V_{ave,max}$=172.7 m/s

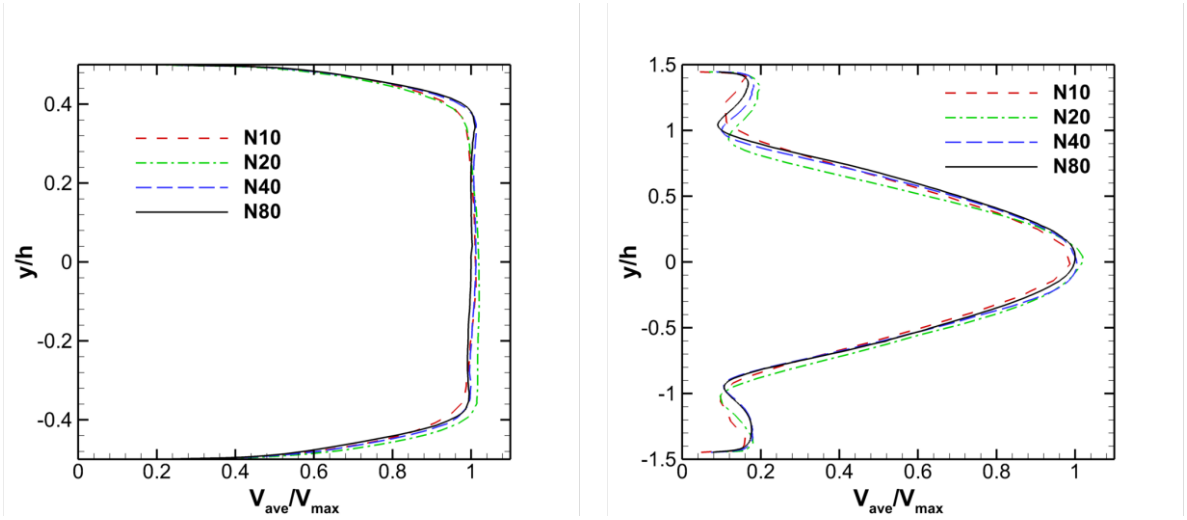

(a) At exit nozzle throat (b) x/h=0

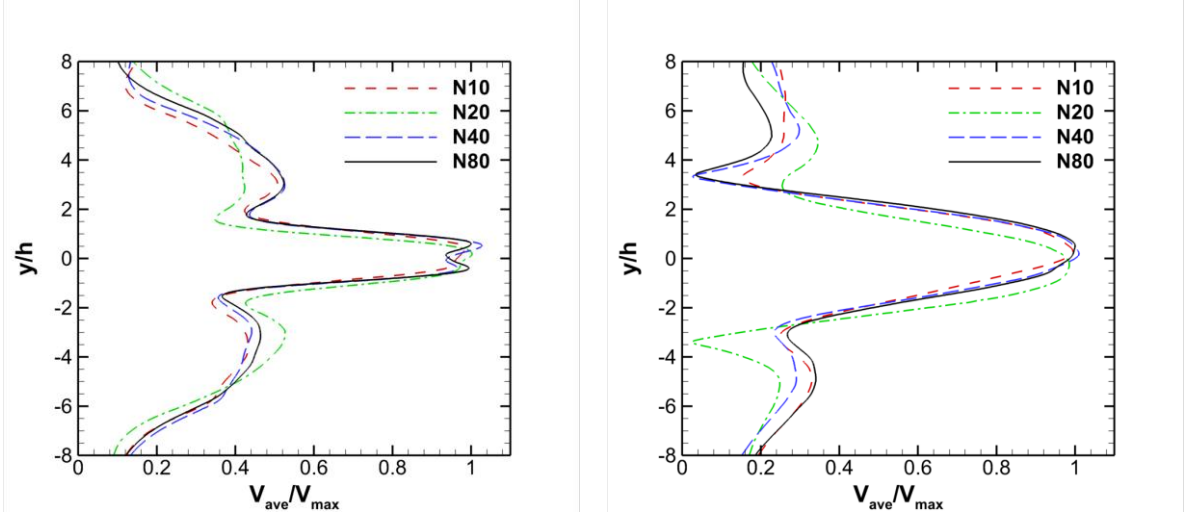

(c) x/h=1 (d) x/h=3

Figure 6. Time-averaged velocity magnitude profiles at various x/h locations.

Preprints (www.preprints.org) | NOT PEER-REVIEWED | Posted: 26 February 2020 doi:10.20944/preprints202002.0384.v1

Peer-reviewed version available at Fluids 2020, 5, 72; doi:10.3390/fluids5020072

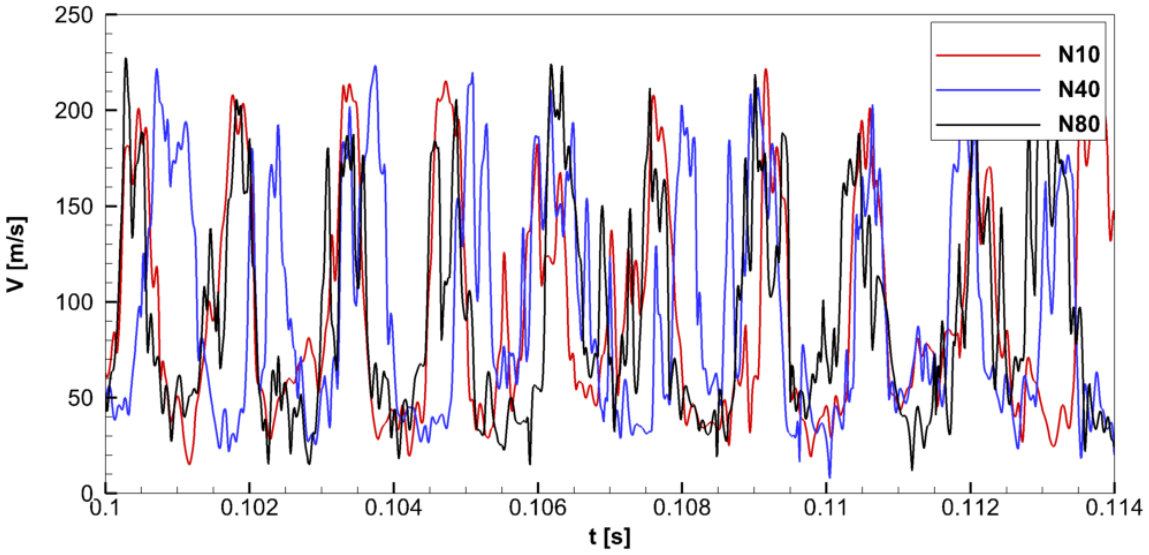

Figure 7. Time history of velocity magnitude at (6 mm, 0) point for various meshes at $\dot{m}$ = 6.8039 g/s.

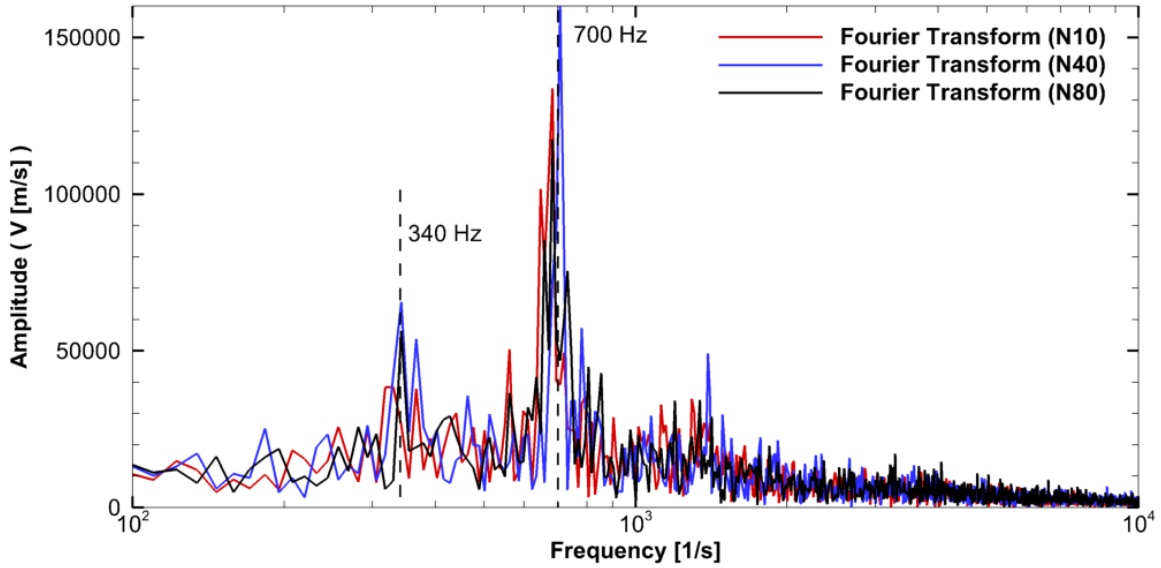

Figure 8. FFT analysis of velocity measurements from various computational meshes ($\dot{m}$ = 6.8039 g/s).

Table 3. Effect of the mesh size on frequency calculations for ($\dot{m}$ = 6.8039 g/s).

Mesh	f (Hz.)	Error (%)
N10	329.6	-3.6
N20	366.2	7.1
N40	341.8	0.0
N80	341.8	0.0

To evaluate the effect of mesh resolution on the time-accurate solutions and jet oscillation frequency, a time history of velocity magnitude is recorded at the downstream of the SWJ actuator exit. The time history of velocity at (6 mm, 0) for 0.006 seconds (600 data points) are shown in Figure 7 for the coarse, fine, and finest meshes. The figure shows that the maximum and minimum velocities are similar. However, there is a slight frequency difference between the signals. For a quantitative comparison, a fast Fourier transform (FFT) analysis is performed on the velocity data to identify the jet oscillation frequency using 8192 data points (0.08 s), as shown in Figure 8 and

oscillations frequencies are listed in Table 3. In the figure, amplitudes are not scaled. Scaling can be done by dividing the amplitude by the data size of 8192. Moreover, 340 Hz and 700 Hz are marked for easy comparison. The peaks showing jet oscillation frequency appeared near 340 Hz, and higher frequency subharmonic is visible in the spectrum. It is found that the jet oscillates at 341.8 Hz when the finest mesh (N80) is used in the simulation. The deviation from the oscillation frequency is 3.6% and 7.1% for N10 and N20 meshes. In a two-dimensional simulation for the same SWJ actuator and flow conditions, the jet oscillation frequency was reported as 346 Hz [9]. The fine mesh (N40) simulation predicted the same oscillation frequency as the finest mesh. As a result of this section, it is found that the fine mesh (N40) generates similar results as the finest mesh (N80), and therefore it will be employed for the rest of this study.

3.2. Effect of Mass Flow Rate

The sweeping jet (SWJ) actuator produces a spanwise oscillating jet. Sweeping jet frequency and oscillation angle depend on the geometry of the SWJ actuator and mass flow rate entering through the inlet. To shed light on the complex flow physics of the SWJ actuator, time-accurate flow simulations are performed for various mass flow rates, as listed in Table 1. The numerical model described in Section 2 is used for the simulations. Time accurate calculations are performed for 0.1 seconds (10,000 time-steps) for initial transients convect away from the computational domain, and the jet establishes bi-stable oscillating motion. Subsequently, time accurate simulations run for 0.10 seconds (10,000 time-steps) to generate a database from which statistically converged flow quantities analyzed. Figure 9 shows the time-averaged velocity magnitude and static pressure along the SWJ actuator symmetry axis (x-axis) for varying mass flow rates. In the time-averaged velocity field, the maximum velocity happens downstream of the exit nozzle throat because of the oscillatory motion of the jet. In the figure, the location of the throat is marked with a gray dashed line. When the actuator pressurized with a mass flow rate of 6.8039 (g/s), the averaged jet speed at exit throat reaches 148.03 m/s, which is also used to non-dimensionalize the velocity profiles in Figure 3-a. In this case, the maximum jet flow speed is observed as 172.66 m/s at the downstream of the exit nozzle throat. The decay of the velocity magnitude exhibits a similar trend along the x-axis. Time-averaged static pressure sharply decreases in the diverging section of the exit nozzle and reaches a plateau.

Time-averaged velocity profiles, the SWJ actuator exit nozzle throat, and various downstream locations are compared for several mass flow rates, as shown in Figure 10. In the figure, the velocities are non-dimensionalized by the throat velocity of 148.03 m/s for the mass flow rate of 6.8039 g/s. A double peak in velocity profile becomes visible in Figure 10-c (x/h=1) for mass flow rates larger than 4.5359 g/s where the peak velocity is 40% less than the mass flow rate of 6.8339 g/s. Although the peak velocities increase with the mass flow rate, the high-speed jet width seems not affected and remained constant for x/h = 1 and 3 stations. Figure 11 shows the root mean square error (RMSE) velocity profiles at x/h = 0 and 1. The RMSE plots show the double peak of the velocity profiles for all mass flow rates indicating the oscillatory behavior of the jet. Moreover, the velocity profile peaks are not located above and below the centerline, which reveals that the oscillating jet spends more time than the centerline.

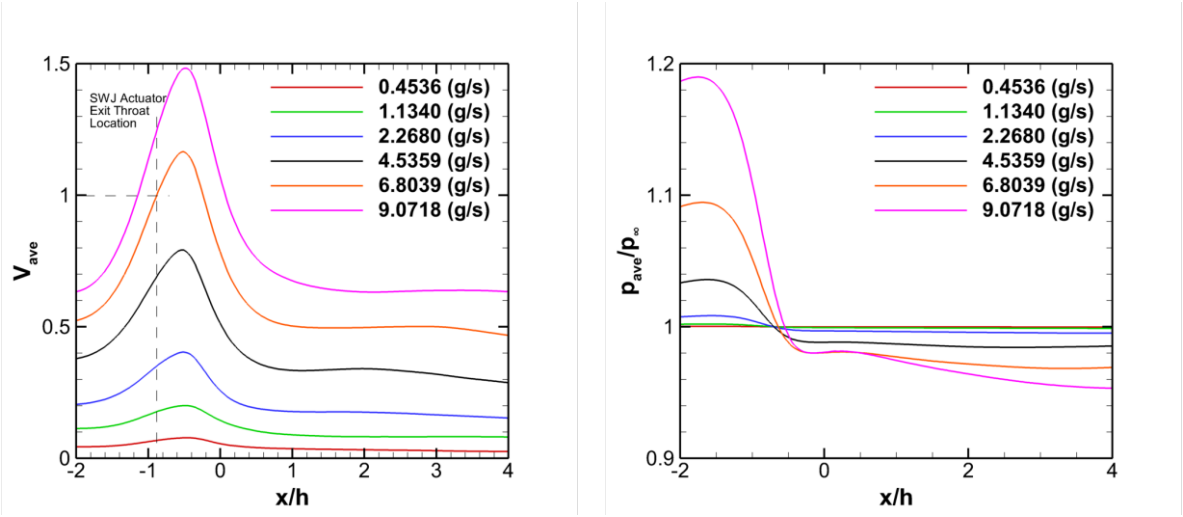

(a) (b)

Figure 9. Time-averaged velocity and static pressure ratio along the centerline at different mass flow rates. For the mass flow rate of 6.8039 (g/s), the maximum value of averaged velocity magnitude at the throat is 148.03 m/s. The $V_{ave,max}$ realizes downstream of the throat and is equal to 172.66 m/s.

To calculate the jet oscillation frequency, time histories of velocity magnitude are sampled at point (6mm, -10 mm) for the mass flow rates given in Table 1. Figure 12 shows the velocity histories for mass flow rates of 6.8039, 9.0718, and 11.3398 g/s. The plots show the data for 14 ms, which provides a time history of five periods for the mass flow rate of 6.8039 g/s. High and low-velocity regions are indicating a jet-on and -off behavior of the oscillation jet at the sampling point. Moreover, high-velocity regions become narrower with increasing mass flow rate. It indicates that the jet oscillation frequency is increasing. Also, the peak velocity of the jet increases with increasing mass flow rate. Figure 13 shows the results of FFT analysis for velocity magnitudes presented in Figure 12. FFT calculations are performed using the Tecplot visualization tool, and 8,192 samples are used for each case. The sample size scales amplitude. The analysis results show the jet oscillation frequency and high-frequency fluctuations. The calculation results are compared with experimental and numerical data available in the literature. The relationship between the jet oscillation frequency and mass flow rate is modeled using a linear regression line of $f = 40.5\dot{m} + 39.9$ where $R^2 = 0.983$. Both 3D-URANS and 3D lattice Boltzmann simulation (LBS) estimate slightly higher frequencies compared to experimental measurements.

Figure 15 shows the jet oscillation frequency with respect to the total to ambient static pressure ratio. The figure reveals two distinct linear frequency responses to the pressure ratio. In the figure solid vertical line shows the Mach number of 0.4 to separate incompressible and compressible flow conditions. Jet oscillation frequency switches from an incompressible linear response to a compressible linear response, which has a smaller slope. The effect of compressibility is not visible in Figure 14.

Preprints (www.preprints.org) | NOT PEER-REVIEWED | Posted: 26 February 2020 doi:10.20944/preprints202002.0384.v1

Peer-reviewed version available at Fluids 2020, 5, 72; doi:10.3390/fluids5020072

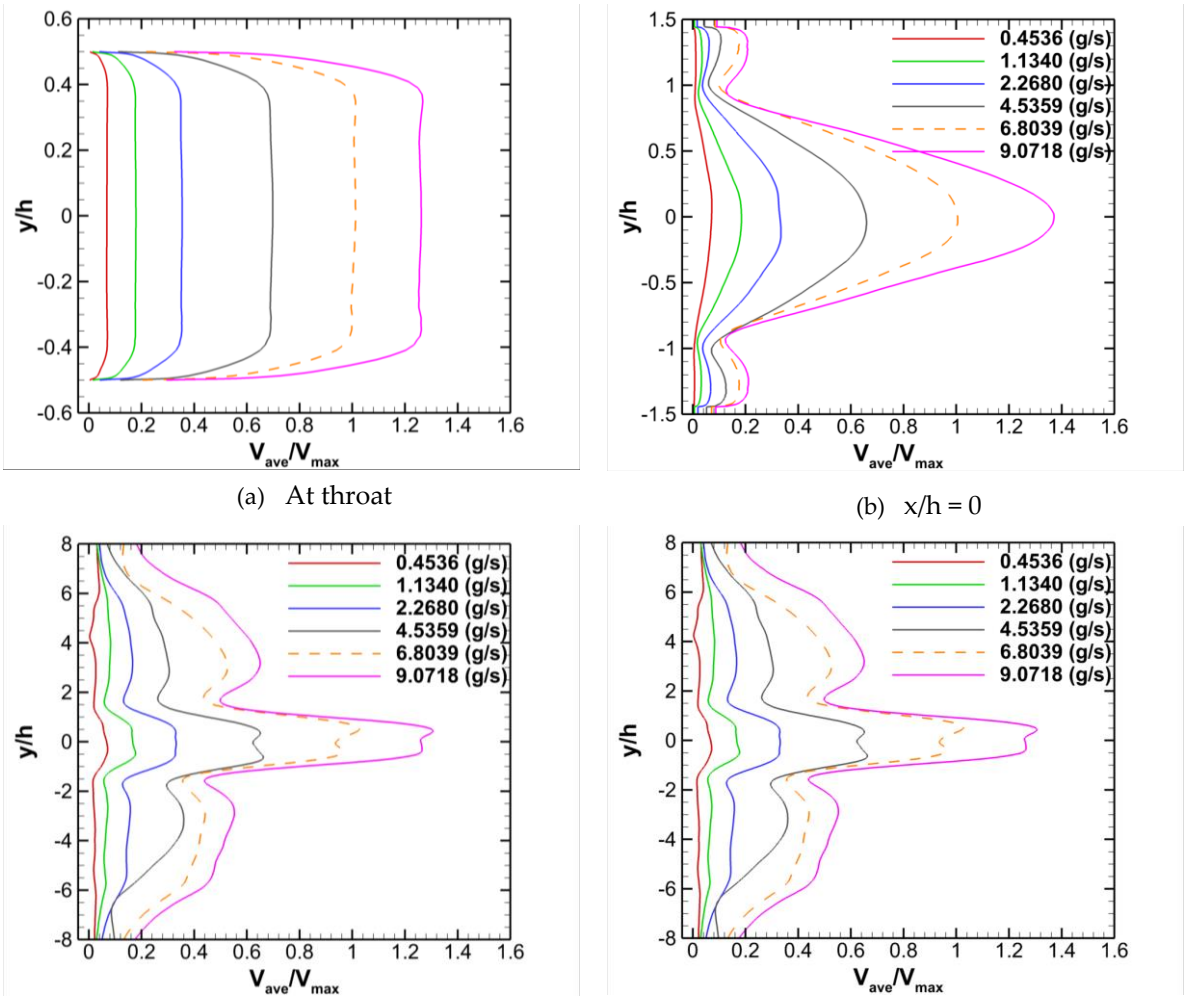

(a) At throat (b) x/h = 0

(c) x/h = 1 (d) x/h = 3

Figure 10. Comparison of mean velocity profiles at various downstream locations. For mass flow rate of 6.8039 (g/s), the maximum value of averaged velocity magnitude at throat is 148.03 m/s, at x/h=0 is 115.67 m/s, at x/h =1 is 79.32 m/s and at x/h=3 is 74.08 m/s.

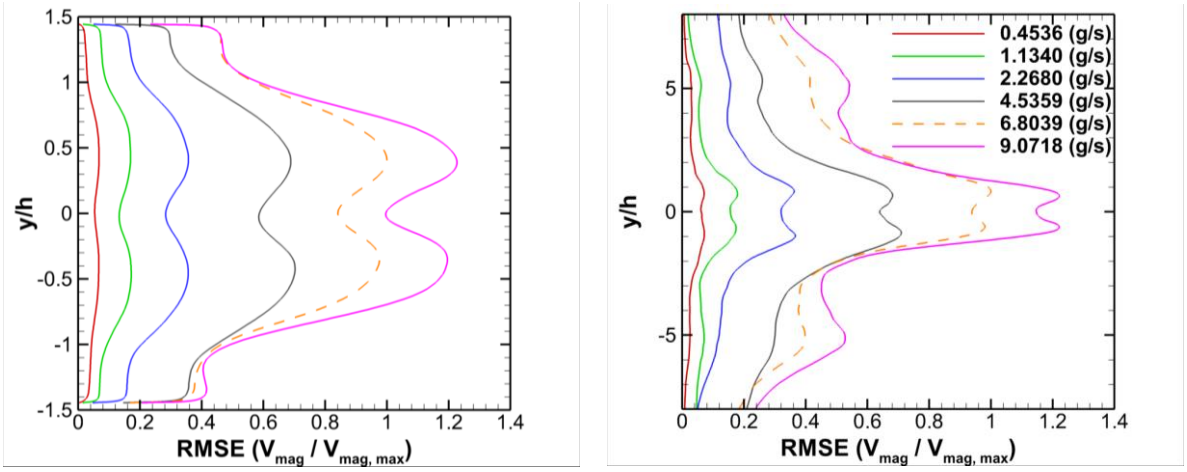

(a) x/h = 0 (b) x/h = 1

Figure 11. Comparison of RMSE velocity magnitude profiles at x/h=0 and x/h=1. The maximum value of RMSE velocity magnitude at x/h=0 is 102.1 m/s x/h =1 is 84.6 m/s for the mass of flow rate of 6.8039 g/s.

Preprints (www.preprints.org) | NOT PEER-REVIEWED | Posted: 26 February 2020 doi:10.20944/preprints202002.0384.v1

Peer-reviewed version available at Fluids 2020, 5, 72; doi:10.3390/fluids5020072

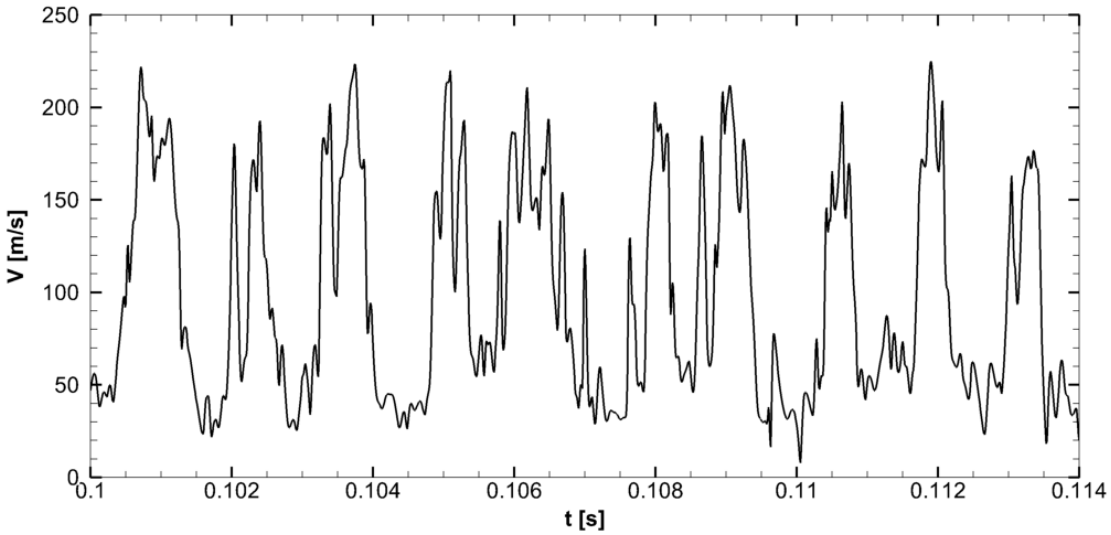

(a) $\dot{m}$ = 6.8039 (g/s)

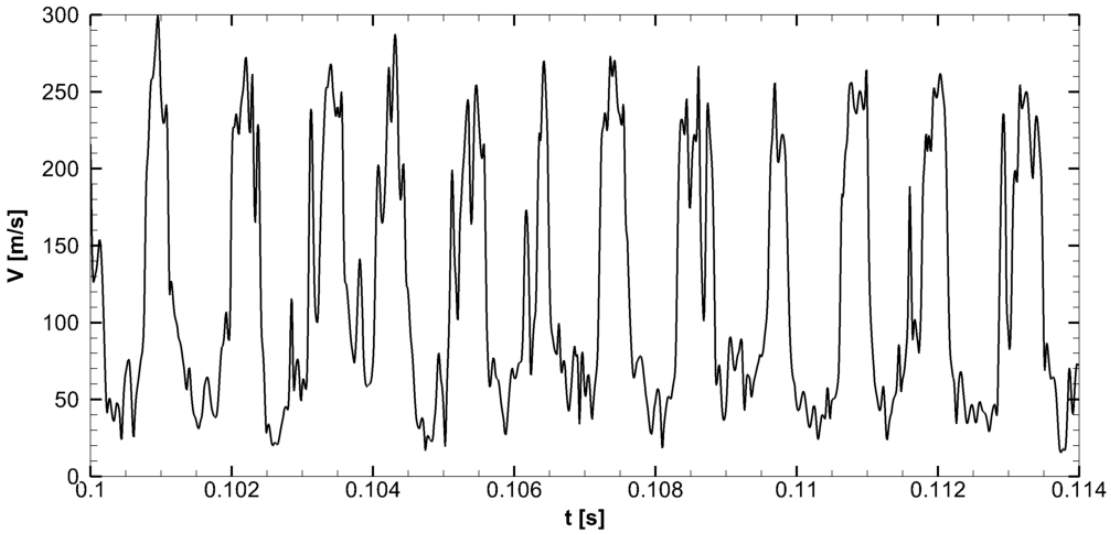

(b) $\dot{m}$ = 9.0718 (g/s)

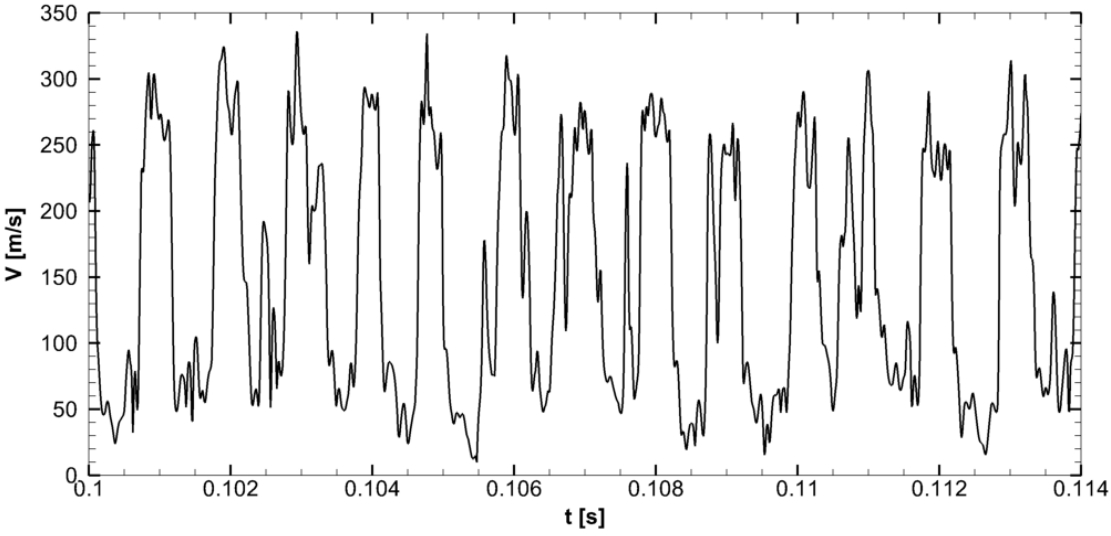

(c) $\dot{m}$ = 11.3398 (g/s)

Figure 12. Time history of velocity magnitude at (6 mm, -10mm).

Preprints (www.preprints.org) | NOT PEER-REVIEWED | Posted: 26 February 2020 doi:10.20944/preprints202002.0384.v1

Peer-reviewed version available at Fluids 2020, 5, 72; doi:10.3390/fluids5020072

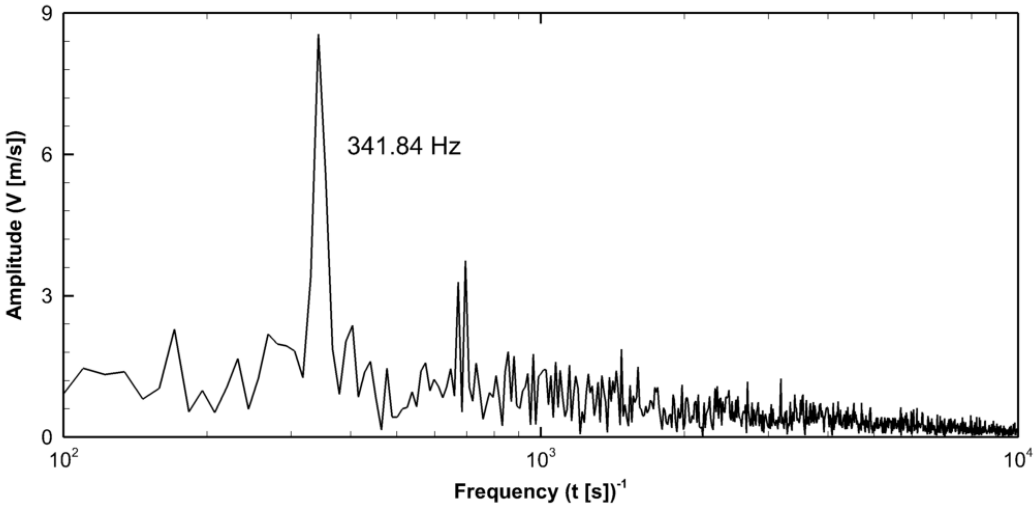

(a) $\dot{m}$ = 6.8039 (g/s)

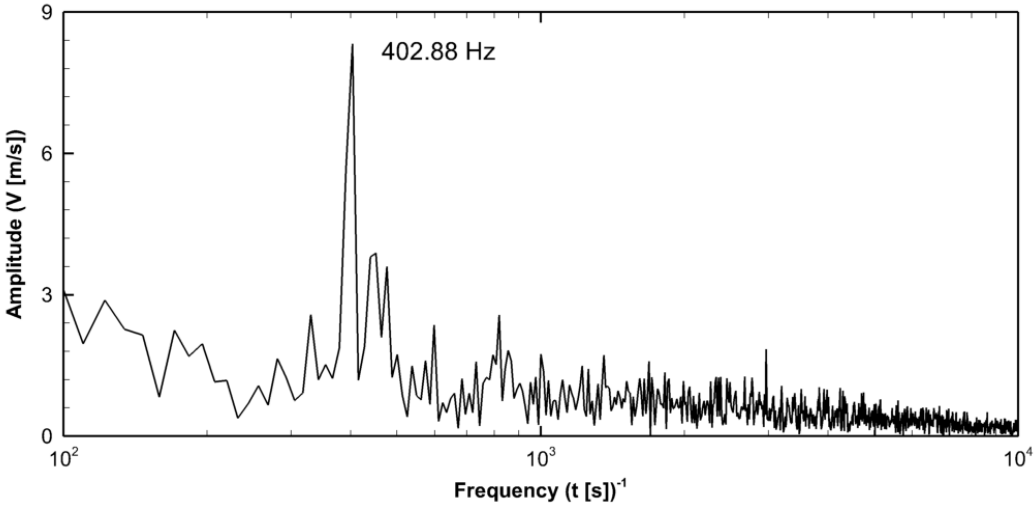

(b) $\dot{m}$ = 9.0718 (g/s)

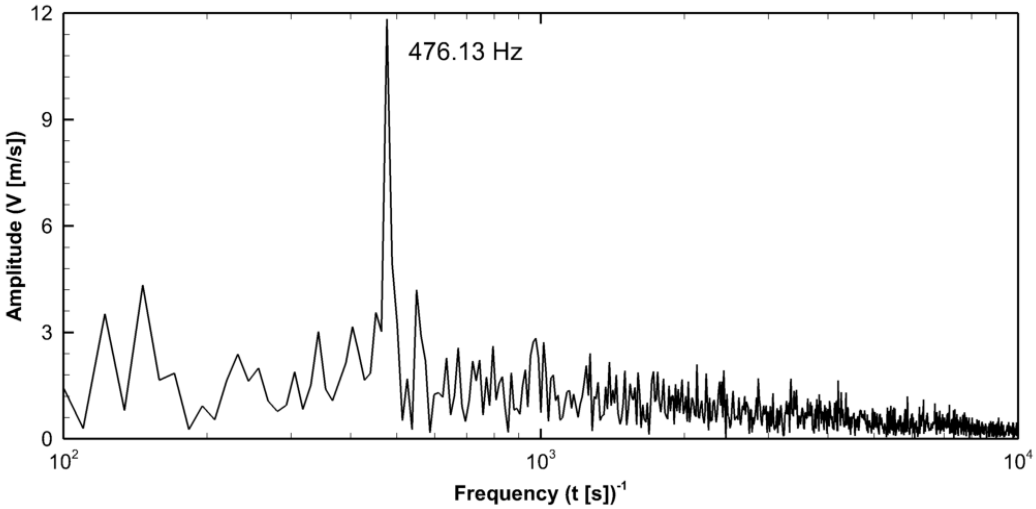

(c) $\dot{m}$ = 11.3398 (g/s)

Figure 13. FFT analysis results of the time history of velocity magnitude recorded at (6 mm, -10 mm) for various mass flow rates.

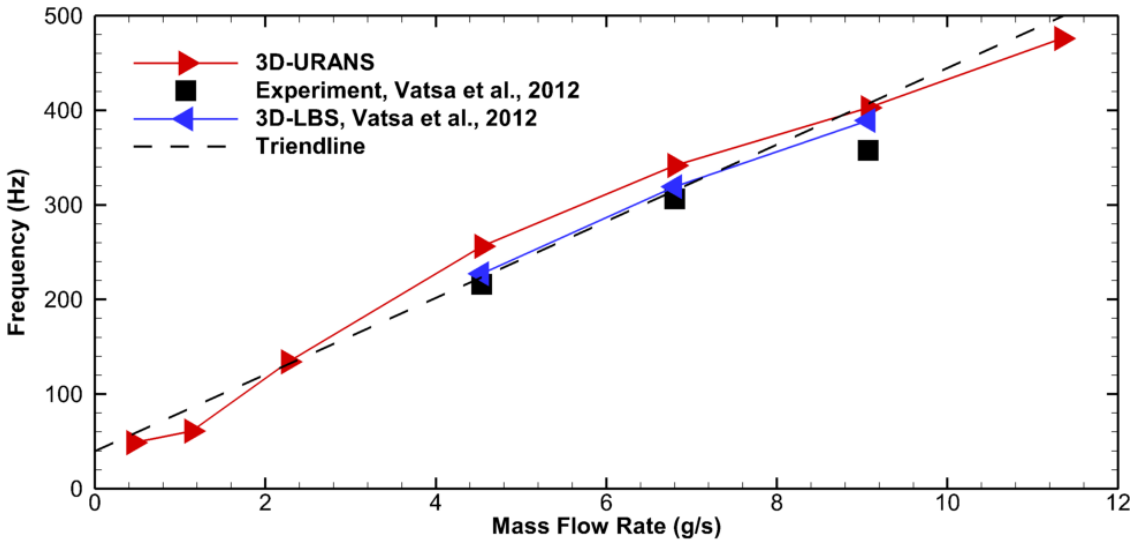

Figure 14. Jet oscillation frequency for increasing mass flow rate.($f = 40.5\dot{m} + 39.9$ $R^2 = 0.983$).

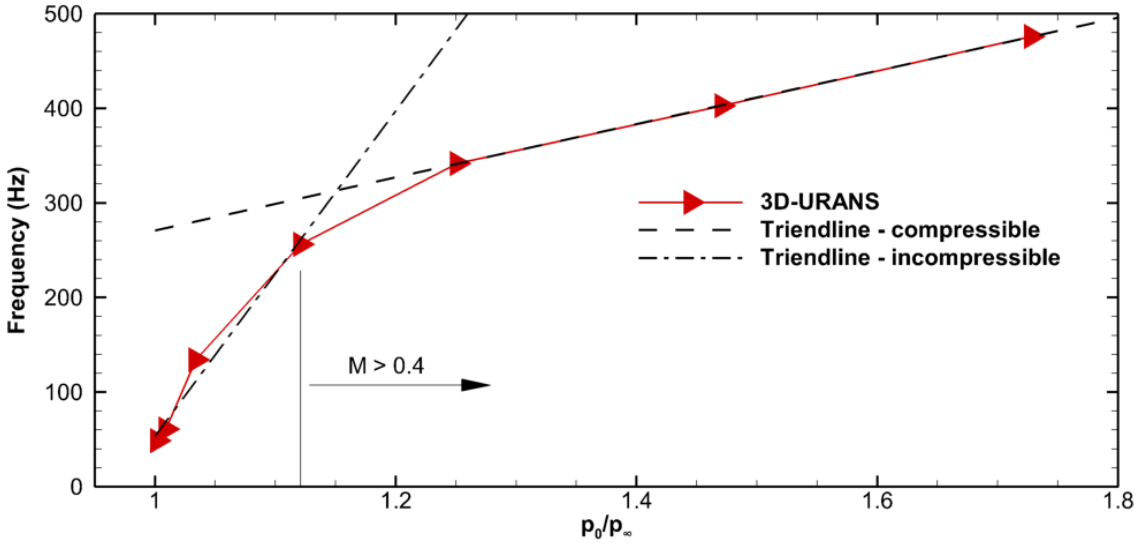

Figure 15. Jet oscillation frequency for incompressible and compressible subsonic flows.

4. Conclusions

In this study, the time-accurate flow field of an SWJ actuator is numerically investigated using three-dimensional unsteady Reynolds-Averaged Navier-Stokes (3D-URANS) model with Ansys Fluent v17. Time accurate 3D-URANS simulations are performed for a practical range of mass flow rates providing flow conditions ranging from subsonic incompressible to compressible flows. The actuator geometry is represented using an automated unstructured mesh with 2 million control volumes. Unstructured hexagonal mesh elements are used to describe complex geometric details for accurate simulation of fully turbulent compressible flows. The jet oscillation frequency is predicted for all of the operating conditions, and a linear relationship between the mass flow rate and the jet oscillation frequency is found ($f = 40.5\dot{m} + 39.9$, $R^2 = 0.983$). The results from the numerical model are compared with experimental and numerical data available in the literature, and a good agreement is found. Moreover, the results showed that there is two distinct linear frequency response of the SWJ actuator in subsonic incompressible and compressible flow regimes.

Acknowledgments: This work of the authors is supported partially by Oklahoma State University, Khalifa University and Korea Advanced Institute of Science and Technology.

References

1. Anders, S.G.; Sellers, WL; Washburn, A.E. Active flow control activities at NASA langley. In Proceedings of the 2nd AIAA Flow Control Conference; 2004.
2. Whalen, E.A.; Spoor, M.; Vijgen, P.M.; Tran, J.; Shmilovich, A.; Lin, J.C.; Andino, M. Full-scale Flight Demonstration of an Active Flow Control Enhanced Vertical Tail. In Proceedings of the 8th AIAA Flow Control Conference; American Institute of Aeronautics and Astronautics: Reston, Virginia, 2016.
3. Lin, J.C.; Andino, M.Y.; Alexander, M.G.; Whalen, E.A.; Spoor, M.A.; Tran, J.T.; Wygnanski, I.J. An overview of active flow control enhanced vertical tail technology development. In Proceedings of the 54th AIAA Aerospace Sciences Meeting; American Institute of Aeronautics and Astronautics Inc, AIAA, 2016.
4. Stouffer, R.D. Liquid Oscillator Device, US Patent 4,508,267 1985.
5. BEALE, RB; LAWLER, MT Development of a Wall-Attachment Fluidic Oscillator Applied To Volume Flow Metering. In *Flow: Its measurement and control in science and industry*; 1974; Vol. 1, pp. 989–996.
6. Wang, H.; Beck, SBM; Priestman, GH; Boucher, R.F. Fluidic pressure pulse transmitting flowmeter. *Chem. Eng. Res. Des.* **1997**, *75*, 381–391.
7. Lucas, N.; Taubert, L.; Woszidlo, R.; Wygnanski, I.; McVeigh, M.A. Discrete sweeping jets as tools for separation control. In *4th AIAA Flow Control Conference*; Fluid Dynamics and Co-located Conferences; AIAA Paper 2008-3868, 2008 ISBN 9781563479427.
8. Tewes, P.; Taubert, L.; Wygnanski, I. On the use of sweeping jets to augment the lift of a λ-wing. In *28th AIAA Applied Aerodynamics Conference*; Fluid Dynamics and Co-located Conferences; AIAA Paper 2010-4689, 2010; Vol. 1 ISBN 9781617389269.
9. Kara, K. Numerical simulation of a sweeping jet actuator. In Proceedings of the 34th AIAA Applied Aerodynamics Conference; American Institute of Aeronautics and Astronautics: Reston, Virginia, 2016; p. 3261.
10. Slupski, B.J.; Kara, K. Effects of geometric parameters on performance of sweeping jet actuator. In Proceedings of the 34th AIAA Applied Aerodynamics Conference; American Institute of Aeronautics and Astronautics: Reston, Virginia, 2016.
11. Duda, B.; Wessels, M.; Fares, E.; Vatsa, V. Unsteady flow simulation of a sweeping jet actuator using a Lattice-Boltzmann method. In Proceedings of the 54th AIAA Aerospace Sciences Meeting; 2016; Vol. 0, p. 1818.
12. Melton, L.T.P.; Koklu, M.; Andino, M.; Lin, J.C.; Edelman, L. Sweeping jet optimization studies. In Proceedings of the 8th AIAA Flow Control Conference; 2016; p. 4233.
13. Koklu, M. Effect of a coanda extension on the performance of a sweeping-jet actuator. *AIAA J.* **2016**, *54*, 1125–1128.
14. Koklu, M.; Owens, L.R. Comparison of sweeping jet actuators with different flow-control techniques for flow-separation control. *AIAA J.* **2017**, *55*, 848–860.
15. Jurewicz, B.; Kara, K. Effects of Feedback Channels and Coanda Surfaces on the Performance of Sweeping Jet Actuator. In Proceedings of the AIAA SciTech Forum - 55th AIAA Aerospace Sciences Meeting; American Institute of Aeronautics and Astronautics: Reston, Virginia, 2017.
16. Aram, S.; Lee, Y.T.; Shan, H.; Vargas, A. Computational fluid dynamic analysis of fluidic actuator for active flow control applications. *AIAA J.* **2018**, *56*, 111–120.

17. Park, T.; Kara, K.; Kim, D. Flow structure and heat transfer of a sweeping jet impinging on a flat wall. *Int. J. Heat Mass Transf.* **2018**, *124*, 920–928.
18. Meng, Q.; Chen, S.; Li, W.; Wang, S. Numerical investigation of a sweeping jet actuator for active flow control in a compressor cascade. In Proceedings of the Proceedings of the ASME Turbo Expo; 2018; Vol. 2A-2018.
19. Woszidlo, R.; Nawroth, H.; Raghu, S.; Wygnanski, I.J. Parametric study of sweeping jet actuators for separation control. In Proceedings of the 5th Flow Control Conference; AIAA Paper 2010-4247, 2010.
20. Phillips, E.; Wygnanski, I.J.; Menge, P.M.; Taubert, L. Passive and Active Leading Edge devices on a simple swept back wing. In Proceedings of the AIAA Aviation 2019 Forum; 2019; p. 3393.
21. Aram, S.; Shan, H. Computational analysis of interaction of a sweeping jet with an attached crossflow. In Proceedings of the AIAA Journal; 2019; Vol. 57, pp. 682–695.
22. Jentzsch, M.; Taubert, L.; Wygnanski, I. Using sweeping jets to trim and control a tailless aircraft model. In Proceedings of the AIAA Journal; 2019; Vol. 57, pp. 2322–2334.
23. Wen, X.; Liu, J.; Li, Z.; Zhou, W.; Liu, Y. Flow dynamics of sweeping jet impingement upon a large convex cylinder. *Exp. Therm. Fluid Sci.* **2019**, *107*, 1–15.
24. Kim, D.J.; Jeong, S.; Park, T.; Kim, D. Impinging sweeping jet and convective heat transfer on curved surfaces. *Int. J. Heat Fluid Flow* **2019**, *79*.
25. Sushanth Gowda, BC; Vinuth, N.; Poornananda, T.; Dhanush, GJ; Paramesh, T. Internal flow analysis on sweeping jet actuator. *Int. J. Recent Technol. Eng.* **2019**, *8*, 296–304.
26. Meng, Q.; Du, X.; Chen, S.; Wang, S. Numerical Study of Dual Sweeping Jet Actuators for Corner Separation Control in Compressor Cascade. *J. Therm. Sci.* **2019**.
27. Chen, S.; Li, W.; Meng, Q.; Zhou, Z.; Wang, S. Effects of a sweeping jet actuator on aerodynamic performance in a linear turbine cascade with tip clearance. *Proc. Inst. Mech. Eng. Part G J. Aerosp. Eng.* **2019**, *233*, 4468–4481.
28. Wen, X.; Liu, J.; Kim, D.; Liu, Y.; Kim, K.C. Study on three-dimensional flow structures of a sweeping jet using time-resolved stereo particle image velocimetry. *Exp. Therm. Fluid Sci.* **2020**, *110*.
29. Woszidlo, R.; Wygnanski, I. Parameters governing separation control with sweeping jet actuators. In *29th AIAA Applied Aerodynamics Conference 2011*; Fluid Dynamics and Co-located Conferences; AIAA Paper 2011-3172, 2011 ISBN 9781624101458.
30. Koklu, M.; Melton, L.P. Sweeping jet actuator in a quiescent environment. In Proceedings of the 43rd Fluid Dynamics Conference; 2013.
31. Seele, R.; Graff, E.; Lin, J.; Wygnanski, I. Performance enhancement of a vertical tail model with sweeping jet actuators. In Proceedings of the 51st AIAA Aerospace Sciences Meeting including the New Horizons Forum and Aerospace Exposition 2013; AIAA Paper 2013-0411, 2013.
32. Gärtlein, S.; Woszidlo, R.; Ostermann, F.; Nayeri, C.N.; Paschereit, C.O. The time-resolved internal and external flow field properties of a fluidic oscillator. In Proceedings of the 52nd Aerospace Sciences Meeting; American Institute of Aeronautics and Astronautics Inc., 2014; pp. 1–15.
33. Koklu, M.; Owens, L.R. Flow separation control over a ramp using sweeping jet actuators. In Proceedings of the AIAA AVIATION 2014 -7th AIAA Flow Control Conference; AIAA Paper 2014-2367, 2014.
34. Andino, M.Y.; Lin, J.C.; Washburn, A.E.; Whalen, E.A.; Graff, E.C.; Wygnanski, I.J. Flow separation control on a full-scale vertical tail model using sweeping jet actuators. In Proceedings of the 53rd AIAA Aerospace Sciences Meeting; 2015; p. 785.

35. Peters, C.J.; Miles, R.B.; Burns, R.A.; Bathel, B.F.; Jones, G.S.; Danehy, P.M. Femtosecond laser tagging characterization of a sweeping jet actuator operating in the compressible regime. In Proceedings of the 32nd AIAA Aerodynamic Measurement Technology and Ground Testing Conference; 2016; pp. 1–22.
36. DeSalvo, M.; Whalen, E.; Glezer, A. High-lift enhancement using fluidic actuation. In Proceedings of the 48th AIAA Aerospace Sciences Meeting Including the New Horizons Forum and Aerospace Exposition; 2010.
37. Seele, R.; Tewes, P.; Woszidlo, R.; McVeigh, M.A.; Lucas, N.J.; Wygnanski, I.J. Discrete sweeping jets as tools for improving the performance of the V-22. *J. Aircr.* **2009**, *46*, 2098–2106.
38. Cerretelli, C.; Wuerz, W.; Gharaibah, E. Unsteady separation control on wind turbine blades using fluidic oscillators. *AIAA J.* **2010**, *48*, 1302–1311.
39. Seifert, A.; Stalnov, O.; Sperber, D.; Arwatz, G.; Palei, V.; David, S.; Dayan, I.; Fono, I. Large trucks drag reduction using active flow control. In Proceedings of the 46th AIAA Aerospace Sciences Meeting and Exhibit; 2008; pp. 115–133.
40. Woszidlo, R.; Stumper, T.; Nayeri, C.N.; Paschereit, C.O. Experimental study on bluff body drag reduction with fluidic oscillators. In Proceedings of the 52nd Aerospace Sciences Meeting; American Institute of Aeronautics and Astronautics Inc., 2014.
41. Kara, K.; Kim, D.; Morris, P.J. Flow-separation control using sweeping jet actuator. *AIAA J.* **2018**, *56*, 4604–4613.
42. Seele, R.; Graff, E.; Gharib, M.; Taubert, L.; Lin, J.; Wygnanski, I. Improving rudder effectiveness with sweeping jet actuators. In Proceedings of the 6th AIAA Flow Control Conference 2012; AIAA Paper 2012-3244, 2012.
43. Koklu, M. Effects of sweeping jet actuator parameters on flow separation control. In Proceedings of the AIAA Journal; 2018; Vol. 56, pp. 1–11.
44. Hirsch, D.; Gharib, M. Schlieren visualization and analysis of sweeping jet actuator dynamics. *AIAA J.* **2018**, *56*, 2947–2960.
45. Ott, C.; Gallas, Q.; Delva, J.; Lippert, M.; Keirsbulck, L. High frequency characterization of a sweeping jet actuator. *Sensors Actuators, A Phys.* **2019**, *291*, 39–47.
46. Horne, W.C.; Burnside, NJ. Acoustic study of a sweeping jet actuator for active flow control applications. In Proceedings of the 22nd AIAA/CEAS Aeroacoustics Conference, 2016; American Institute of Aeronautics and Astronautics Inc, AIAA, 2016.
47. Seo, J.H.; Zhu, C.; Mittal, R. Flow physics and frequency scaling of sweeping jet fluidic oscillators. *AIAA J.* **2018**, *56*, 2208–2219.
48. Vatsa, V.; Koklu, M.; Wygnanski, I. Numerical Simulation of Fluidic Actuators for Flow Control Applications. In Proceedings of the 6th AIAA Flow Control Conference; American Institute of Aeronautics and Astronautics: Reston, Virigina, 2012.
49. Kara, K. Numerical Study of Internal Flow Structures in a Sweeping Jet Actuator. In Proceedings of the 33rd AIAA Applied Aerodynamics Conference; American Institute of Aeronautics and Astronautics: Reston, Virginia, 2015; pp. 1–18.